



# Noble-metal-free Ni<sub>3</sub>C cocatalysts decorated CdS nanosheets for high-efficiency visible-light-driven photocatalytic H<sub>2</sub> evolution

Song Ma<sup>a,1</sup>, Yanping Deng<sup>a,1</sup>, Jun Xie<sup>a,b</sup>, Kelin He<sup>a,b</sup>, Wei Liu<sup>a</sup>, Xiaobo Chen<sup>c</sup>, Xin Li<sup>a,b,\*</sup>

<sup>a</sup> College of Materials and Energy, South China Agricultural University, Guangzhou 510642, PR China

<sup>b</sup> College of Forestry and Landscape Architecture, Key Laboratory of Energy Plants Resource and Utilization, Ministry of Agriculture, South China Agricultural University, Guangzhou 510642, PR China

<sup>c</sup> Department of Chemistry, University of Missouri – Kansas City, Kansas City, MO 64110, USA

## ARTICLE INFO

### Keywords:

Photocatalytic hydrogen evolution  
CdS Nanosheets  
Noble-metal-free Ni<sub>3</sub>C cocatalysts  
Heterojunctions  
Charge kinetics

## ABSTRACT

In this work, Ni<sub>3</sub>C nanoparticles (NPs, 0 D) were for the first time used as H<sub>2</sub>-evolution cocatalysts to modify CdS nanosheets (NSs, 2 D) to achieve the high-efficiency photocatalytic H<sub>2</sub> evolution under visible light irradiation. The photocatalytic H<sub>2</sub>-evolution activities of the Ni<sub>3</sub>C/CdS hybrid NSs were tested under 350 W Xe lamp irradiation ( $\lambda \geq 420$  nm) with a sacrificial agent. The results proved that Ni<sub>3</sub>C NPs were efficient cocatalysts for photocatalytic H<sub>2</sub> evolution over CdS NSs. The CdS-1% Ni<sub>3</sub>C hybrid NSs exhibited the highest photocatalytic H<sub>2</sub>-evolution rates of 357  $\mu\text{mol h}^{-1}$  in 0.25 M Na<sub>2</sub>S-Na<sub>2</sub>SO<sub>3</sub> and 450.5  $\mu\text{mol h}^{-1}$  in lactic acid, which were approximately 7.76 and 4.79 times higher than that of bare CdS NSs, corresponding to the apparent quantum yields of 7.58% and 8.72% at 420 nm, respectively. Clearly, the Ni<sub>3</sub>C NPs serve as H<sub>2</sub>-evolution electrocatalysts either in acidic or basic media. It is believed that the noble-metal-free Ni<sub>3</sub>C cocatalyst NPs on the surface of CdS NSs can effectively increase the visible-light absorbance, promote the charge carriers separation and transfer, improve the surface H<sub>2</sub>-evolution kinetics, thus achieving the obviously boosted hydrogen evolution. It is hoped that this study could contribute to the further investigation in exploiting the low-priced, high efficiency and environmentally friendly noble-metal-free cocatalysts for photocatalytic H<sub>2</sub> evolution.

## 1. Introduction

Hydrogen production by photocatalytic water splitting represents one of the most promising approaches for energy storage and clean fuel generation in a post fossil age [1]. Since the groundbreaking report by Fujishima and Honda about the photoelectrochemical splitting of water on TiO<sub>2</sub> electrodes using UV light in 1972 [2], various inorganic and organic semiconductors have been available for photocatalytic hydrogen evolution from water splitting [1,3,4]. To maximally utilize the visible-light region in the solar spectrum, cadmium sulfide (CdS) with an adequate narrow band gap (2.4 eV) and proper thermodynamic conduction band potential has been considered to be an excellent visible-light-responsive semiconductor for solar H<sub>2</sub> production [5]. Although much progress has been achieved in the field of photocatalytic H<sub>2</sub> evolution over CdS, it is still a huge challenge to rationally design the efficient and robust CdS-based H<sub>2</sub>-evolution systems for the practical applications, owing to the poor separating efficiency of photo-excited charges and the undesired deactivation processes driven by photo-generated holes [6]. Accordingly, to tremendously improve the

photocatalytic activity and stability of CdS toward H<sub>2</sub> production, a large number of modification approaches have been widely proposed during the past few decades, including fabricating nanostructured CdS [7–10], constructing semiconductor heterojunctions [11–16], designing Z-scheme systems [17–21], coupling with nano-carbons [5,22–25], loading cocatalysts [26–32], exploiting solid solution and surface doping [33]. Among these pathways, fabricating nanostructured CdS and loading cocatalysts were considered to be two most attractive methods to significantly improve the photocatalytic activity.

On the one hand, various nanostructured CdS photocatalysts, including quantum dots [31,32], nanoparticles [17], nanorod/nanowires [26,27,29,34], nanoflowers [7], etc. have been extensively constructed to achieve the highly boosted photocatalytic H<sub>2</sub> evolution, owing to the unique nanoscale effects for promoting the charge separation and exposing more active sites [35]. However, to the best of our knowledge, there are few works focusing on applications of ultrathin 2D CdS nanosheet-based photocatalysts in the photocatalytic H<sub>2</sub> evolution [19,36–38], which might be due to complicated fabrication procedures. In 2007, Bao et al. synthesized nanoporous CdS nanosheets with sizes

\* Corresponding author at: College of Forestry and Landscape Architecture, South China Agricultural University, Guangzhou 510642, PR China.

E-mail addresses: [Xinliscou@yahoo.com](mailto:Xinliscou@yahoo.com), [Xinli@scau.edu.cn](mailto:Xinli@scau.edu.cn) (X. Li).

<sup>1</sup> These authors contributed equally.

up to 60 nm and an average thickness of about 9 nm by a two-step aqueous route, involving the first precipitation of nanoporous  $\text{Cd}(\text{OH})_2$  intermediates and a subsequent  $\text{S}^{2-}/\text{OH}^-$  ion-exchange conversion of the obtained  $\text{Cd}(\text{OH})_2$  used as self-template [39]. The as-obtained nanoporous CdS nanostructures loaded with monodisperse 3–5 nm Pt nanocrystals exhibited the highest apparent quantum yield of about 60.34% at 420 nm. In 2013, Zhang and his coworkers reported that the ultrathin CdS nanosheets (NSs) with a thickness of 4 nm could be facilely fabricated through a simple solvothermal and solution-phase ultrasonic exfoliation approach using lamellar CdS-amine inorganic-organic hybrid nanosheets as starting materials [40]. These CdS ultrathin nanosheets show excellent activity and good stability for photocatalytic  $\text{H}_2$  evolution under visible light irradiation in sacrificial agent solution. More recently, Zhukovskiy et al. developed a new strategy to fabricate the high-quality, thickness-controlled CdS nanosheets (NSs) with discrete thicknesses of 1.50–2.16 nm and lateral dimensions on the order of  $90 \text{ nm} \times 20 \text{ nm}$  through the thermal decomposition of cadmium diethyldithiocarbamate in octadecene [38]. The resulting CdS NSs supported Ni NP (a diameter of 6 nm) could achieve the apparent quantum yields of 25% for photocatalytic hydrogen generation in water/ethanol mixtures. In this direction, these reports open new ways to fabricate various 2D CdS nanosheet-based composite photocatalysts, such as 2D-2D coupling CdS-MoS<sub>2</sub> [36] and mediator-free Z-scheme CdS-WO<sub>3</sub> systems [19] for different applications.

On the other hand, it is generally accepted that the noble metals, such as Pt, Au and Ag, have been extensively photo-deposited on the nanostructured CdS photocatalysts to achieve very high quantum efficiency for photocatalytic  $\text{H}_2$  generation due to the promoted charge separation and improved  $\text{H}_2$ -evolution kinetics [41]. However, the high price and scarcity of noble metals significantly restrict their extensive applications. Recently, to construct the highly active  $\text{H}_2$ -evolution systems without any noble metals, numerous earth-abundant robust cocatalysts have been revealed to boost the photocatalytic  $\text{H}_2$ -evolution activity over CdS, such as Ni [38,42], nickel complex [43], MoS<sub>2</sub> [44–49], Cu<sub>2</sub>S [50], Cu<sub>2</sub>MoS<sub>4</sub> [51], NiS [28,52], WS<sub>2</sub> [53,54], Ni<sub>2</sub>P [55,56], CoP<sub>x</sub> [57,58], Co<sub>3</sub>N [59], Ni<sub>3</sub>C [60], CoO<sub>x</sub> [27,61] and Ni(OH)<sub>2</sub> [62,63]. Especially, tremendous efforts have demonstrated that the transition metal carbides, such as WC [64], Mo<sub>2</sub>C [65] and Ti<sub>2</sub>C<sub>3</sub> Mxene [66], are promising cocatalysts for efficient photocatalytic  $\text{H}_2$  generation. More interestingly, a series of nickel carbides, such as high-index faceted dendritic NiCo<sub>0.2</sub> nanosheets [67], Ni<sub>3</sub>C nanocrystals encased in graphene nanoribbons [68] and Ni<sub>3</sub>C nanoparticles embedded in a porous carbon network [69] have been found to exhibit superior electrocatalytic activity for  $\text{H}_2$  production in acidic or basic media. Notably, to the best of our knowledge, there have been no studies regarding the applications of Ni<sub>3</sub>C as cocatalysts for promoting photocatalytic  $\text{H}_2$  evolution over CdS. To this end, it is of great interest to exploit the really promising and earth-abundant Ni<sub>3</sub>C cocatalyst for improving photocatalytic  $\text{H}_2$  evolution over CdS.

Accordingly, it is extremely desirable that the scrupulous integration and design of nanostructured CdS and suitable earth-abundant cocatalysts could fundamentally reduce carrier migration distance from bulk to its surface, increase the specific surface area and effective HER active sites, accelerate  $\text{H}_2$ -evolution kinetics, and decrease activation energy barrier for  $\text{H}_2$  evolution [42], thus achieving the robust and active photocatalytic  $\text{H}_2$  evolution. Herein, earth-abundant Ni<sub>3</sub>C NPs as cocatalysts were for the first time loaded onto CdS NSs to markedly boost their photocatalytic  $\text{H}_2$ -evolution activity. The Ni<sub>3</sub>C/CdS NSs composite photocatalysts were successfully synthesized by a simple grind method, which exhibited much better photocatalytic  $\text{H}_2$ -evolution activity than that of pure CdS NSs either in 0.25 M Na<sub>2</sub>S-Na<sub>2</sub>SO<sub>3</sub> or lactic acid aqueous solution under visible light irradiation. The possible mechanism for improving the photocatalytic activity of Ni<sub>3</sub>C/CdS NSs composite photocatalysts was proposed in this study.

## 2. Experimental

### 2.1. Preparation of photocatalysts

#### 2.1.1. Materials

All materials used in this research were of analytical grade and used as received, including cadmium chloride ( $\text{CdCl}_2 \cdot 2.5\text{H}_2\text{O}$ ), sulfur powder, diethylenetriamine (DETA), nickel acetate anhydrous ( $\text{Ni}(\text{Ac})_2$ ), and oleylamine.

#### 2.1.2. Synthesis of CdS NSs

The CdS NSs were synthesized by a facile solvothermal method [40]. 10 mmol of sulfur powder was added into 60 mL of DETA with vigorous stirring until it dissolved completely. Then, 1.6 mmol of  $\text{CdCl}_2 \cdot 2.5\text{H}_2\text{O}$  was dispersed in the mixture with stirring and sonication. After that, the suspension was transferred into a 100 mL Teflon-lined autoclave, heated at 80 °C for 48 h, and then naturally cooled to room temperature. The pale yellow precipitate was collected by centrifugation (8000 rpm, 5 min) and washed three times with deionized water and ethanol, respectively. Finally, it was dried at 80 °C for 10 h in a vacuum drying oven.

#### 2.1.3. Synthesis of Ni<sub>3</sub>C NPs

The Ni<sub>3</sub>C NPs were synthesized by a reported method [70]. 2 mmol of  $\text{Ni}(\text{Ac})_2$  and 14.1 mL of oleylamine were mixed into a 100 mL three-neck round-bottom flask. The mixture was stirred magnetically under a nitrogen atmosphere. Then, it was heated to 250 °C and kept this temperature for 2 h. 30 mL of acetone was added into the mixture after cooling to room temperature. The Ni<sub>3</sub>C NPs were collected by centrifugation (5000 rpm, 15 min) and dried at 60 °C for 10 h in an oven.

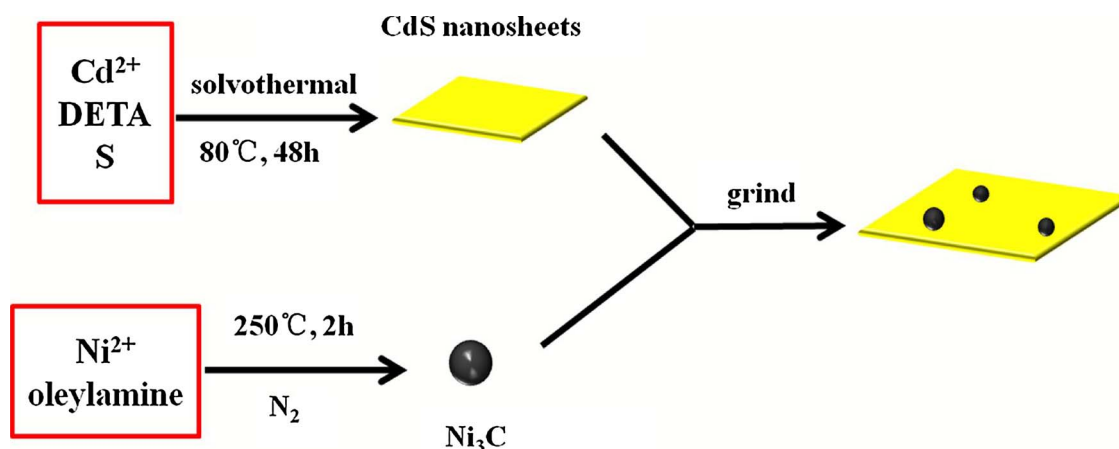
#### 2.1.4. Synthesis of Ni<sub>3</sub>C/CdS NSs composites

In a typical synthesis method, 400 mg CdS NSs and 4 mg Ni<sub>3</sub>C NPs powders were grounded together in an agate mortar for 1 h and stored for further characterization. The whole synthesis process was shown in Scheme 1.

The obtained composite powder with 1 wt% Ni<sub>3</sub>C NPs was denoted as CdS-1.0%Ni<sub>3</sub>C. The other composites with different contents of Ni<sub>3</sub>C were prepared according to the same method. The other Ni<sub>3</sub>C/CdS NSs composites with 0.5 wt%, 1.5 wt% and 2 wt% Ni<sub>3</sub>C NPs, were denoted as CdS-0.5%Ni<sub>3</sub>C, CdS-1.5%Ni<sub>3</sub>C and CdS-2.0%Ni<sub>3</sub>C, respectively.

### 2.2. Characterization

Power X-ray (XRD) patterns were collected on a MSAL-XD2 diffractometer using a Cu K $\alpha$  radiation source (operated at 36 kV and 30 mA,  $\lambda = 1.54056 \text{ \AA}$ ) to determine the crystal phase of CdS NSs, Ni<sub>3</sub>C NPs, and their composites. The morphology images of the samples were obtained by scanning electron microscopy (SEM), transmission electron microscopy (TEM) and high-resolution transmission electron microscopy (HRTEM) using a JEM-2100HR (200 kV, Japan) operated at 200 kV. The UV–vis diffuse reflection spectra (UV–vis DRS) were recorded with a Daojin UV-2550PC diffuse reflectance spectroscopy, 100% BaSO<sub>4</sub> was used as the reference. X-ray photoelectron spectroscopy (XPS) data was performed with a VG ESCALAB250 surface analysis system using a 300 W Al K $\alpha$  X-ray radiation source (5 mA and 15 kV). All the binding energies were calibrated using the C 1s level at 284.8 eV as the reference. The pure CdS NSs and CdS-1.0%Ni<sub>3</sub>C samples were degassed at 120 °C before nitrogen absorption measurements. A Brunauer–Emmett–Teller (BET) method was used to determine the specific surface area in the relative pressure ( $P/P_0$ ) range of 0.05–0.99. The pore-size distributions were researched from the desorption branches of the isotherms using the Barrett–Joyner–Halenda (BJH) method. The nitrogen adsorption volume at the relative pressure ( $P/P_0$ ) of 0.99 was used to investigate the pore volume and the mean pore diameter. The photoluminescence (PL) spectra of the photocatalysts were



Scheme 1. Schematically illustrating the formation of  $\text{Ni}_3\text{C}/\text{CdS}$  NSs photocatalysts.

recorded on a LS 50B (Perkin Elmer, Inc., USA) with an excitation wavelength of 230 nm. The time-resolved decay curves of the as-fabricated samples were recorded with a FLS920 fluorescence lifetime spectrophotometer (Edinburgh Instruments, UK) under the excitation of a hydrogen flash lamp with the wavelength at 325 nm (nF900; Edinburgh Instruments).

### 2.3. Photocatalytic experiments procedures

The photocatalytic  $\text{H}_2$  evolution was carried out in a 100 mL three-neck flat-bottom Pyrex flask at ambient pressure and temperature. Silicone rubber septum was used to seal the opening of the flask. A 350 W Xe arc lamp with a UV cut-off filter ( $\lambda \geq 420$  nm) was used as the light source to trigger the photocatalytic reaction (19 cm far away from the reactor). The focused light intensity on the flask was ca.  $160 \text{ mW cm}^{-2}$ . In a typical experiment, 25 mg of as-prepared photocatalyst nanopowders were suspended in the reactor containing 80 mL of an aqueous solution of  $\text{Na}_2\text{S}$  (0.25 M) and  $\text{Na}_2\text{SO}_3$  (0.25 M) under constant stirring and ultrasonic bath. Before irradiation, the suspensions of the photocatalysts were bubbled with  $\text{N}_2$  for 30 min to remove the dissolved oxygen to make sure that the system was under anaerobic conditions. 200  $\mu\text{L}$  of evolved gas was collected through the septum and analyzed using an online gas chromatograph (GC-9560, TCD, with Ar as carrier gas) after 1 h of irradiation.

### 2.4. Electrochemical tests

The working electrodes were prepared as this method: 5 mg of photocatalyst powders and 20  $\mu\text{L}$  of 0.25% Nafion solution were added into 2 mL of absolute ethanol to make a slurry, then the mixture solution was ultrasound for 2 h. 500  $\mu\text{L}$  of the mixture solution was injected onto a  $2 \times 3.5 \text{ cm}^2$  fluorine-doped tin-oxide (FTO) glass substrate. The FTO glass substrates were dried under the infrared lamp and calcined in tube furnace at  $150^\circ\text{C}$  for 1 h in a  $\text{N}_2$  gas flow. Finally, the working electrodes were successfully prepared as this method.

Transient photocurrent experiments were conducted on an electrochemical analyzer (BAS100 Instruments) in a standard three-electrode system. The as-prepared working electrodes, Pt electrode and Ag/AgCl (3.5 M KCl) electrode were used as the working electrodes, counter electrode, reference electrode, respectively. 0.1 M  $\text{Na}_2\text{SO}_4$  aqueous solution was used as the electrolyte. A 350 W Xe lamp with a UV cut-off filter ( $\lambda \geq 420$  nm) was used as the light source.

The electrochemical impedance spectra (EIS) of above-mentioned working electrodes in a three-electrode system were obtained by a computer controlled IM6e impedance measurement unit (Zahner Elektrik, Germany) over a frequency range of 0.01–100,000 Hz with an ac amplitude of 10 mV in the dark. 0.1 M  $\text{Na}_2\text{S}$  and 0.02 M  $\text{Na}_2\text{SO}_3$

mixed aqueous solution was used as the electrolyte solution.

The flat-band potential of the working electrodes were tested by the Mott–Schottky (MS) method in the same three-electrode electrochemical system. The measurements were performed over a scanning the electrode potential range of  $-1.0 - 1.2 \text{ V}$  with a scan rate of 50 mV/s in dark, and the impedance-potential characteristics were recorded at a frequency of 1 kHz. 0.1 M  $\text{Na}_2\text{SO}_4$  aqueous solution was used as the electrolyte.

The electrocatalytic hydrogen evolution was tested using a three-electrode cell. Linear sweep voltammetry with a  $5 \text{ mV}^{-1}$  scan rate was performed in 0.5 M  $\text{H}_2\text{SO}_4$  electrolyte solution using a Pt plate as the counter electrode, and Ag/AgCl (saturated KCl) as a reference electrode. The potential values after iR-corrected were normalized to reverse hydrogen electrode (NHE). In 0.5 M  $\text{H}_2\text{SO}_4$  electrolyte solution,  $E(\text{NHE}) = E(\text{Al}/\text{AgCl}) + 0.202 \text{ V}$ . The working electrodes were prepared as follows: 6 mg of photocatalyst was ultrasonically dispersed into 2 mL of deionized water (at least 2 h) and then injected on glassy carbon electrode with 3  $\mu\text{L}$  of the solution. After drying under the infrared lamp, 3  $\mu\text{L}$  of 0.5% Nafion solution (contain 10 vol% ethanol) was then added on top of the photocatalyst layer.

## 3. Results and discussion

### 3.1. The structures and compositions of photocatalysts

X-ray diffraction (XRD) patterns were used to analyze the crystal phase of as-prepared pure and composite photocatalysts. Fig. 1 depicts the power XRD patterns of pure  $\text{Ni}_3\text{C}$  NPs, pure CdS NSs and all  $\text{Ni}_3\text{C}/\text{CdS}$  NSs composites. The standard diffraction patterns of pure  $\text{Ni}_3\text{C}$  NPs and CdS NSs were shown in Fig. 1A and B, respectively. According to the reference and XRD pattern, the crystal phase of as-prepared  $\text{Ni}_3\text{C}$  NPs matches well with the standard hexagonal phase (JCPDS No: 72-1467). As displayed in Fig. 1B, the six characteristic peaks at  $2\theta$  values of  $25.11^\circ$ ,  $26.82^\circ$ ,  $28.47^\circ$ ,  $44.00^\circ$ ,  $48.29^\circ$ , and  $52.16^\circ$  correspond to the diffractions of (100), (002), (101), (110), (103), and (112) planes of hexagonal CdS (JCPDS No: 41-1049) [40]. No diffraction peaks from residues can be detected. The analysis results proved that the well-crystallized hexagonal CdS NSs were successfully synthesized via a solvothermal method. However, no characteristic diffraction peaks of  $\text{Ni}_3\text{C}$  were observed in the XRD pattern of hybrid  $\text{Ni}_3\text{C}/\text{CdS}$  NSs composites because of the small contents of  $\text{Ni}_3\text{C}$  NPs and high dispersion of the  $\text{Ni}_3\text{C}$  NPs in the composites. The existence of  $\text{Ni}_3\text{C}$  NPs in  $\text{Ni}_3\text{C}/\text{CdS}$  NSs composite photocatalysts needs to be further confirmed by other tests.

Transmission electron microscopy (TEM), scanning electron microscopy (SEM) and high-resolution transmission electron microscopy (HRTEM) were further used to investigate the structures and



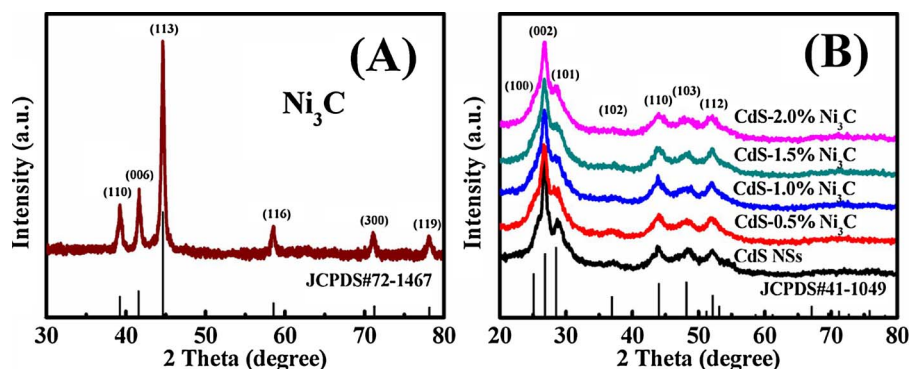


Fig. 1. The XRD patterns of  $\text{Ni}_3\text{C}$  (A) and the  $\text{Ni}_3\text{C}/\text{CdS}$  NSs composites (B).

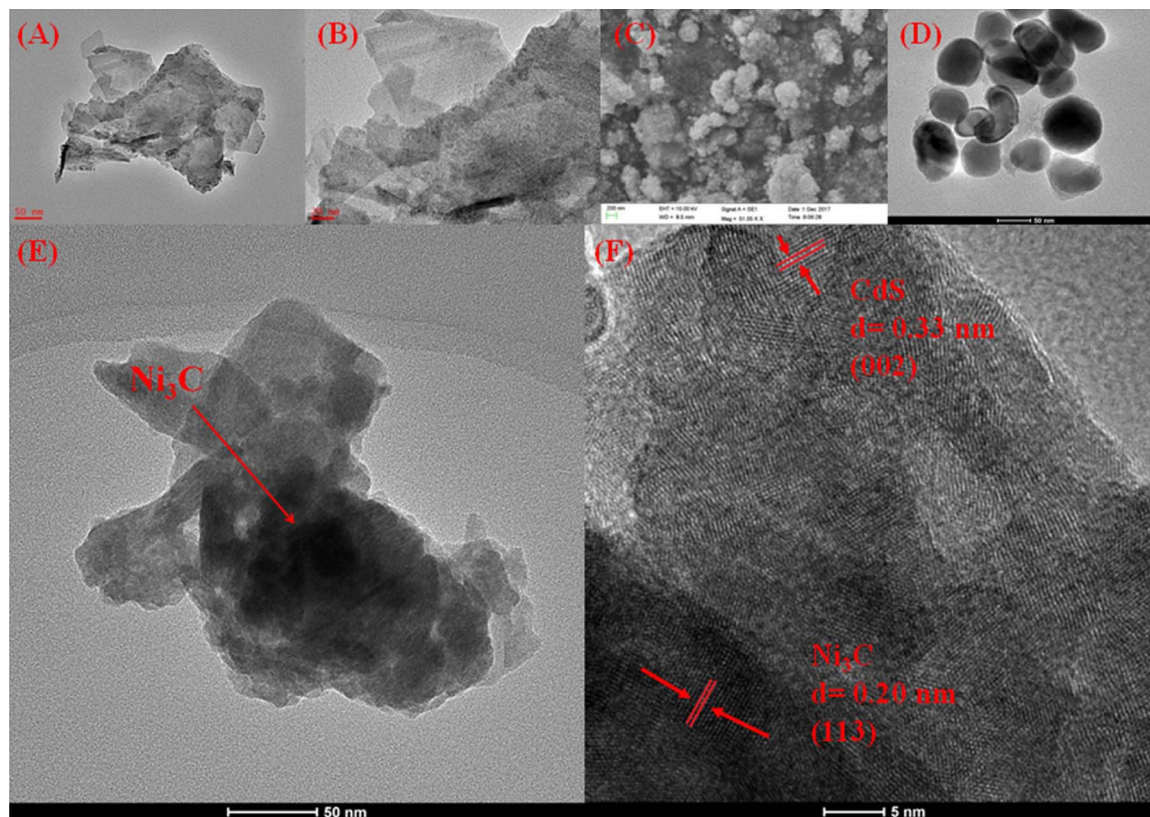


Fig. 2. TEM images of (A,B) CdS NSs, (C) SEM image of  $\text{Ni}_3\text{C}$  NPs, (D) TEM image of  $\text{Ni}_3\text{C}$  NPs, (E) TEM image of CdS-1% $\text{Ni}_3\text{C}$ , (F) HRTEM image of CdS-1% $\text{Ni}_3\text{C}$ .

morphologies of as-prepared  $\text{Ni}_3\text{C}$  NPs, CdS NSs and their composites. Fig. 2A and B shows the well-dispersed CdS NSs with the lateral dimensions of 150–300 nm, which are consistent with our previously reported results [36]. As displayed in Fig. 2C and D, the average grain diameter of  $\text{Ni}_3\text{C}$  NPs was about 50 nm. These results indicated that the CdS NSs and  $\text{Ni}_3\text{C}$  NPs were successfully synthesized via the reported method [40,71,72]. As displayed in Fig. 2C and D, the  $\text{Ni}_3\text{C}$  NPs with the average grain diameter of about 50 nm were uniformly dispersed on the surface of the CdS NSs. Fig. 2E confirms that the evident interfaces between CdS NSs and  $\text{Ni}_3\text{C}$  NPs have been fabricated. Generally speaking, it was well accepted that the intimate contact interface could provide charge transfer and trapping channels for achieving the rapid separation. Furthermore, the HRTEM image of CdS-1.0% $\text{Ni}_3\text{C}$  sample displayed in Fig. 2F shows the lattice fringes with interplanar spacing of 0.33 and 0.20 nm of CdS-1%  $\text{Ni}_3\text{C}$  sample, corresponding to the (002) and (113) plane of the hexagonal CdS (JCPDS No: 41-1049) and  $\text{Ni}_3\text{C}$  (JCPDS No: 72-1467), respectively. It could be observed from Fig. 3A that the energy-dispersive X-ray (EDX) peaks of Cd, S, Ni and C elements were detected on the CdS-1%  $\text{Ni}_3\text{C}$  sample, further indicating the

existence of  $\text{Ni}_3\text{C}$  NPs on the CdS NSs. The HRTEM elemental mapping (Fig. 3B–F) could confirm the co-existence of Cd, S, Ni, and C elements in CdS-1%  $\text{Ni}_3\text{C}$  sample, further indicating the uniform dispersion of  $\text{Ni}_3\text{C}$  on the surface of CdS NSs. All the analysis results suggested that the CdS-1% $\text{Ni}_3\text{C}$  sample with 2D–0D nanoheterostructure was successfully prepared, which was consistent with the above XRD patterns.

X-ray photoelectron spectroscopy (XPS) was employed to further analyze the surface elemental components and oxidation states of the bare CdS NSs and CdS-1.0% $\text{Ni}_3\text{C}$  composite. As displayed in Fig. 4A, the fully scanned spectra indicates the existence of Cd, S, Ni, C and trace amounts of O in CdS-1% $\text{Ni}_3\text{C}$  composites. The oxidation states of the surface elements were verified via the XPS spectrum of Cd 3d, S 2p, Ni 2p and C 1s. Fig. 4B shows that the XPS peaks of Cd 3d centered at 404.3 and 411.1 eV correspond to Cd 3d<sub>5/2</sub> and Cd 3d<sub>3/2</sub>, respectively, confirming the dominant formation of Cd<sup>2+</sup> in CdS NSs and CdS-1%  $\text{Ni}_3\text{C}$  composite [73]. Fig. 4C and F further compares the XPS spectra of S 2p of these two photocatalysts. The S 2p peaks were located at the binding energies of 161.4 and 160.2 eV with a peak separation of 1.2 eV, corresponding to the sulfide in CdS-1% $\text{Ni}_3\text{C}$  composite. In

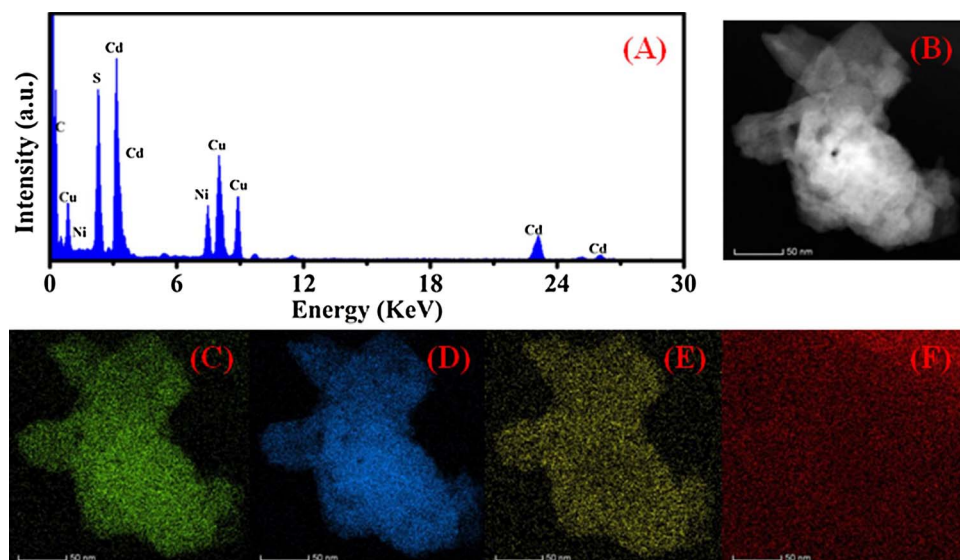


Fig. 3. (A) EDX spectrum of CdS-1%Ni<sub>3</sub>C, and (B–F) the corresponding elemental mapping of CdS-1%Ni<sub>3</sub>C.

addition, it could be obviously observed that the binding energy of S 2p of CdS-1%Ni<sub>3</sub>C shifts toward the higher energy in comparison with that of pure CdS NSs (2p<sub>3/2</sub>, 159.9 eV), which might be attributed to the existence of Ni<sub>3</sub>C in which S interacted with Ni<sup>+</sup>. Moreover, the XPS peaks of the Ni 2p spectrum (Fig. 4D) appeared at 855.2 (Ni 2p<sub>3/2</sub>) and 861.3 eV (Ni 2p<sub>3/2</sub> satellite), corresponding to the dominant oxidation state of Ni<sup>+</sup>, further indicating the presence of pure Ni<sub>3</sub>C phase in the CdS-1%Ni<sub>3</sub>C composite. The C 1s XPS spectrum were divided into three peaks (Fig. 4E). The peaks at 283.1 and 284.8 eV were assigned to the Ni–C bonds and sp<sup>2</sup> hybridized carbon atoms in C–C bonds, respectively. Additionally, the peak of C–O functional group could be observed at 286 eV. All the results further confirmed that the Ni<sub>3</sub>C NPs was successfully loaded on the surface of CdS NSs.

As displayed in Fig. 5, the N<sub>2</sub> adsorption–desorption isotherms and the corresponding pore size distribution curves of pure CdS NSs and CdS-1%Ni<sub>3</sub>C were used to further elucidate the textural property of the obtained two samples nanostructures. Obviously, the type-IV adsorption–desorption isotherms at high relative pressure range could be

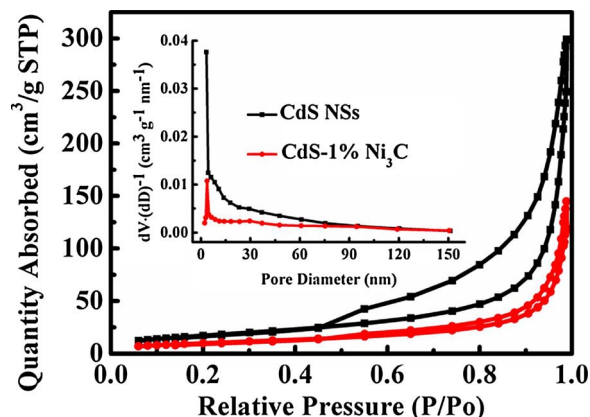


Fig. 5. N<sub>2</sub> adsorption–desorption isotherms and the corresponding pore size distribution curves (inset) of pure CdS NSs and CdS-1%Ni<sub>3</sub>C.

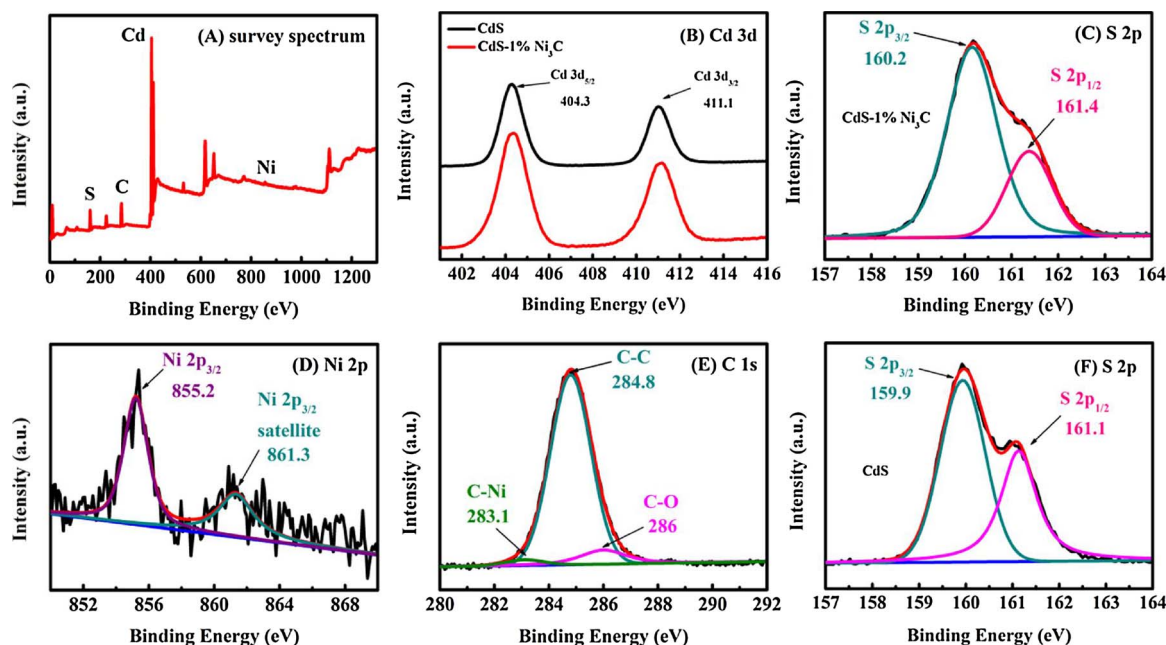


Fig. 4. (A) XPS survey spectrum of the CdS-1%Ni<sub>3</sub>C photocatalyst, (B) Cd 3d of CdS NSs and CdS-1%Ni<sub>3</sub>C photocatalysts, (C) S 2p of CdS-1%Ni<sub>3</sub>C photocatalyst, (D) Ni 2p of CdS-1%Ni<sub>3</sub>C photocatalyst, (E) C 1s of CdS-1%Ni<sub>3</sub>C photocatalyst, (F) S 2p of CdS NSs photocatalyst.



**Table 1**  
Pore structure parameter of pure CdS NSs and CdS-1%Ni<sub>3</sub>C.

Photocatalysts	BET specific surface area (m <sup>2</sup> g <sup>-1</sup> )	Mean pore diameter (nm)	Pore volume (cm <sup>3</sup> g <sup>-1</sup> )
CdS NSs	63.8207	14.0174	0.463962
CdS NSs-1%Ni <sub>3</sub> C	37.2939	19.0205	0.183501

observed for two samples according to the Brunauer–Deming–Deming–Teller classification [74], indicating the presence of the mesoporous structures. Moreover, the distinct type H3 hysteresis loops for these two samples suggested the formation of slit-like pores which were generally associated with the aggregation of plate-like particles. Meanwhile, the DFT pore size distributions for two samples (inset) clearly proved the existence of mesopores and macropores. The other pore structure parameters of two samples were further summarized in Table 1. As shown in Table 1, the BET specific surface area, average pore diameter and pore volume of the CdS NSs are 63.82 m<sup>2</sup> g<sup>-1</sup>, 14.02 nm and 0.46 cm<sup>3</sup> g<sup>-1</sup>, whereas those of CdS-1%Ni<sub>3</sub>C sample are 37.29 m<sup>2</sup> g<sup>-1</sup>, 19.02 nm and 0.18 cm<sup>3</sup> g<sup>-1</sup>. It could be observed that both BET surface area and pore volume of the CdS-1%Ni<sub>3</sub>C composites were much lower than that of pure CdS NSs, but the average pore diameter increased after loading Ni<sub>3</sub>C. These results might be due to that loading Ni<sub>3</sub>C NPs on the surface of CdS NSs leads to the partial filling and blocking of mesoporous, indicating the unobvious roles of BET surface area and pore volume of these two photocatalysts in promoting the photocatalytic H<sub>2</sub> production.

### 3.2. The optical properties of photocatalysts

UV–vis absorption spectra of the pure CdS NSs, Ni<sub>3</sub>C/CdS NSs composite and pure Ni<sub>3</sub>C samples were investigated using a UV–vis diffuse reflectance spectroscopy. The UV–vis absorption spectra and Tauc plots of the photocatalysts were shown in Fig. 6. As was shown in Fig. 6A, the absorption band edges were located at 525 nm for pure CdS NSs and all the Ni<sub>3</sub>C/CdS NSs composites. Interestingly, there was a significantly enhanced absorbance in the visible-light range (> 500 nm) with increasing the content of Ni<sub>3</sub>C NPs. This was consistent with the observed color change of the samples from light yellow to dark green, after a low content of black Ni<sub>3</sub>C NPs was introduced on the surface of the bare CdS NSs (Fig. 6A, inset). The UV–vis absorption spectrum of the Ni<sub>3</sub>C NPs shows no obvious absorption edge in the region ranging from 200 to 800 nm, indicating the narrow band or metallic nature of Ni<sub>3</sub>C NPs. These results suggested that the addition of Ni<sub>3</sub>C NPs could effectively increase the absorbance of visible light and create more available photogenerated carriers, thus enhancing light harvesting and favoring the photocatalytic H<sub>2</sub> evolution. The band gaps for CdS NSs and CdS-1%Ni<sub>3</sub>C could be calculated by the following equation [61]:

$$\alpha = A(h\nu - E_g)^{n/2}/h\nu$$

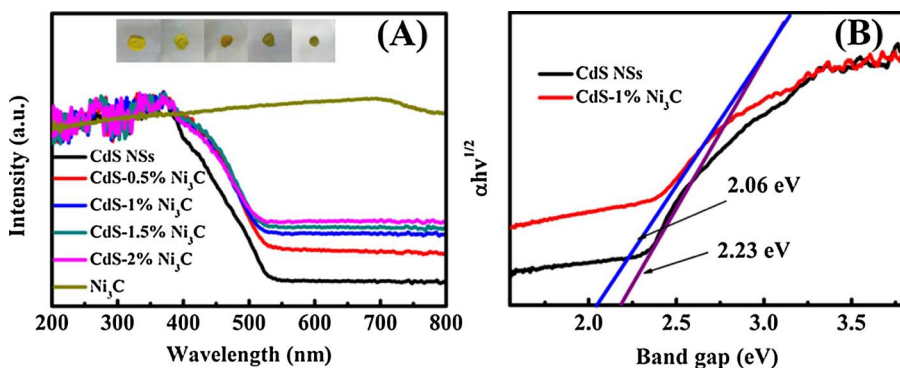


**Fig. 6.** (A) UV–vis absorption spectra of as-prepared samples and the optical images of samples (inset) and (B) Tauc plots of the UV–vis spectra. (For interpretation of the references to colour in this figure legend, the reader is referred to the web version of this article.)

where  $\alpha$ ,  $A$ ,  $h$ ,  $\nu$  and  $E_g$  are the absorption coefficient, proportionality constant, Planck's constant, frequency of the incident light and band energy, respectively, and  $n$  is equal to 1 for the direct transition. The corresponding Tauc plots of the UV–vis spectra were shown in Fig. 6B, where the intercept of the tangent on horizontal axis is the value of the bandgap energies. The band gaps of pure CdS NSs and CdS-1%Ni<sub>3</sub>C were estimated to be 2.23 and 2.06 eV, respectively. These results indicated that the intimate interfacial interactions between Ni<sub>3</sub>C NPs and CdS NSs lead to the narrower band energy of CdS-1%Ni<sub>3</sub>C, thus achieving the enhanced visible-light absorption [75]. Therefore, it is believed that the enhanced absorbance of the Ni<sub>3</sub>C/CdS NSs composites in visible light region might be beneficial for improving the photocatalytic H<sub>2</sub> evolution.

### 3.3. The activities and stabilities of photocatalysts

The photocatalytic H<sub>2</sub>-evolution activity of Ni<sub>3</sub>C/CdS NSs composite with different amounts of Ni<sub>3</sub>C NPs was tested under 350 W Xe lamp irradiation ( $\lambda \geq 420$  nm) using 0.25 mol L<sup>-1</sup> of Na<sub>2</sub>S–Na<sub>2</sub>SO<sub>3</sub> aqueous solution as a sacrificial agent, as shown in Fig. 7. Control experiments showed that no H<sub>2</sub> production could be detected without photocatalysts or irradiation, suggesting that all of these components are crucial for the H<sub>2</sub> production. The time courses of H<sub>2</sub> production over as-prepared photocatalysts (displayed in Fig. 7A) showed a linear increase in the rates of H<sub>2</sub> evolution over all samples during the photocatalytic reactions, which suggested that all samples had excellent photostability under visible-light irradiation. To further compare the H<sub>2</sub>-evolution activity of different samples, the average H<sub>2</sub>-evolution rates over all photocatalyst samples during the whole reactions were calculated and displayed in Fig. 7B. Surprisingly, the pure CdS NSs exhibited much higher photocatalytic H<sub>2</sub>-evolution activity than those previously reported CdS nanoparticles and nanorods [44]. The Ni<sub>3</sub>C/CdS composite photocatalysts with 0–2.0 wt% Ni<sub>3</sub>C NPs showed obvious higher rates of H<sub>2</sub> evolution than pure CdS NSs. An optimum loading content Ni<sub>3</sub>C NPs on the surface of CdS NSs was found to be about 1wt.%. Under optimized conditions, the highest rate of H<sub>2</sub> evolution was 357  $\mu$ mol h<sup>-1</sup> (with apparent quantum efficiency of 7.58% at 420 nm), which was about 7.76 times higher than that of pure CdS NSs (46.2  $\mu$ mol h<sup>-1</sup>). Clearly, the loaded suitable content of Ni<sub>3</sub>C cocatalysts on the CdS NSs could greatly improve the photocatalytic H<sub>2</sub>-evolution activity of CdS NSs, indicating that the Ni<sub>3</sub>C NPs could effectively separate the photogenerated electrons and holes. Notably, the excess Ni<sub>3</sub>C NPs cocatalyst loaded on the CdS NSs could result in a relative decrease in photocatalytic H<sub>2</sub>-evolution activity, which could be attributed to the shielding effects of excess Ni<sub>3</sub>C NPs for the both incident light and the photogeneration of electrons from CdS NSs [24]. It could be seen from Fig. 7C that the H<sub>2</sub>-evolution activity of CdS-1%Ni<sub>3</sub>C was greatly higher than those of pure CdS NSs, CdS-1%Pt and the physically mixed sample of CdS NSs and 1% Ni<sub>3</sub>C in the same sacrificial agent solution, further indicating the important function of Ni<sub>3</sub>C NPs in enhancing the photocatalytic activity of binary Ni<sub>3</sub>C/CdS NSs composites.

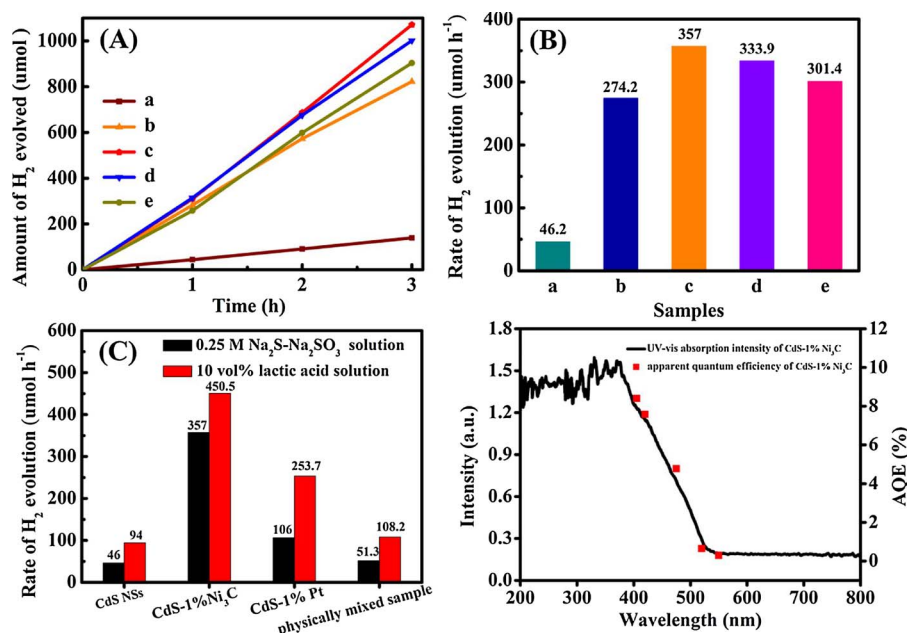


Fig. 7. (A) Reaction time courses and (B) the average rate of H<sub>2</sub> evolution over different photocatalysts in aqueous solution: (a) CdS NSs, (b) CdS-0.5%Ni<sub>3</sub>C, (c) CdS-1%Ni<sub>3</sub>C, (d) CdS-1.5%Ni<sub>3</sub>C and (e) CdS-2%Ni<sub>3</sub>C. (C) Comparison of H<sub>2</sub> evolution activities of CdS-1%Ni<sub>3</sub>C, CdS-1%Pt and physical mixed sample of CdS NSs and 1% Ni<sub>3</sub>C in 0.25 M Na<sub>2</sub>S-Na<sub>2</sub>SO<sub>3</sub> aqueous solution or 10 vol% lactic acid solution. (D) UV-vis absorption spectrum of CdS-1%Ni<sub>3</sub>C and the apparent quantum efficiencies of CdS-1%Ni<sub>3</sub>C in 0.25 M Na<sub>2</sub>S-Na<sub>2</sub>SO<sub>3</sub> aqueous solution with different wavelength. Reaction conditions: catalyst, 25 mg; 80 mL sacrificial agent solution; light source, Xenon lamp (350 W) with a UV cut-off filter ( $\lambda \geq 420$  nm).

More interestingly, in lactic acid as the sacrifice agent, the optimum CdS-1%Ni<sub>3</sub>C shows much higher average rate of H<sub>2</sub> evolution than that in Na<sub>2</sub>S-Na<sub>2</sub>SO<sub>3</sub> aqueous solution. The corresponding apparent quantum efficiency for H<sub>2</sub> evolution could reach 8.72% at 420 nm. As shown in Fig. 7D, the apparent quantum efficiencies of CdS-1%Ni<sub>3</sub>C were observed in 0.25 M Na<sub>2</sub>S-Na<sub>2</sub>SO<sub>3</sub> aqueous solution at different wavelength. The apparent quantum efficiencies at 405, 420, 475, 520, 550 nm were evaluated to 8.41%, 7.58%, 4.79%, 0.62%, 0.28%, respectively. The variation trends of apparent quantum efficiencies were in good agreement with UV-vis absorption spectrum of CdS-1%Ni<sub>3</sub>C, further indicating the important role of visible light absorption in determining the photocatalytic H<sub>2</sub>-evolution activity.

Owing to the importance of the photostability of a given composite photocatalyst in improving their practical application, the cycling tests were also performed to further confirm the long-term stability and reproducibility of the CdS-1%Ni<sub>3</sub>C NSs photocatalyst for H<sub>2</sub> evolution. As displayed in Fig. 8, the H<sub>2</sub>-evolution rate over CdS-1%Ni<sub>3</sub>C gradually decreased after every reaction cycle. After five consecutive reaction cycles, the CdS-1%Ni<sub>3</sub>C sample lost 35% of the original photocatalytic H<sub>2</sub>-evolution activity under visible light illumination. Moreover, it should be pointed out that similar phenomena were also verified over CdS loaded with other noble metal-free cocatalysts [53]. The activity loss might be attributed to both the photocorrosion of CdS NSs by the holes and a slow fall-off of the Ni<sub>3</sub>C NPs cocatalyst from CdS NSs [76]. The results clearly suggest that the photostability of Ni<sub>3</sub>C/CdS NSs

composites could be further improved through constructing the tight Ni<sub>3</sub>C/CdS interfaces or the protective layer for future practical applications.

### 3.4. The charge-separation performances

Photoluminescence (PL) emission spectra were used to further study the charge-carriers recombination and electronic transition behavior of the Ni<sub>3</sub>C/CdS NSs photocatalysts under the light irradiation with a particular wavelength. It is generally believed that the lower intensity of PL signal indicates the improved charge trapping and efficient transferring [77,78]. The PL spectra of CdS NSs and CdS-1%Ni<sub>3</sub>C were tested at room temperature with an excitation wavelength of 230 nm. As observed in Fig. 9A, the pure CdS NSs and CdS-1%Ni<sub>3</sub>C exhibit an emission peak centered at 525 nm, corresponding to the recombination of electron-hole pairs in CdS NSs. After loading Ni<sub>3</sub>C NPs onto the surface of CdS NSs, the emission peak intensity of CdS-1%Ni<sub>3</sub>C was much lower than that of pure CdS NSs, indicating that an efficient transfer of photogenerated electrons could be achieved from CdS NSs to Ni<sub>3</sub>C NPs. These results suggested that loading Ni<sub>3</sub>C NPs onto the surface of CdS NSs could obviously facilitate the separation and transfer processes of photo-generated charge carriers, which play the important roles in determining the photocatalytic H<sub>2</sub>-evolution activity.

To further understand the improved separation efficiency of photogenerated charge carriers, the transient photocurrent response (I-t curves) of pure CdS NSs and CdS-1%Ni<sub>3</sub>C composite photocatalysts were measured for several visible light on-off cycles. As shown in Fig. 9B, the CdS-1%Ni<sub>3</sub>C composite exhibited much higher photocurrent density than pure CdS NSs under the same condition, suggesting that a higher separation efficiency of the photogenerated electron-hole pairs was achieved after loading Ni<sub>3</sub>C on the surface of CdS NSs. Therefore, more photogenerated electrons could be created and transferred to yield hydrogen. These above results further demonstrated that loading Ni<sub>3</sub>C NPs on the surface of CdS NSs could greatly promote the improved photocatalytic activity by increasing the charge transfer and separation efficiency. Compared with pure CdS NSs, despite the CdS-1% Ni<sub>3</sub>C photocatalyst exhibits the 7.76-fold enhancement in the photocatalytic activity, the corresponding photocurrent density just exhibits less three times higher than that of pure CdS NSs, indicating there is no direct linear relation between the photocurrent density and photocatalytic H<sub>2</sub>-evolution activity. The photocurrent density is just one of

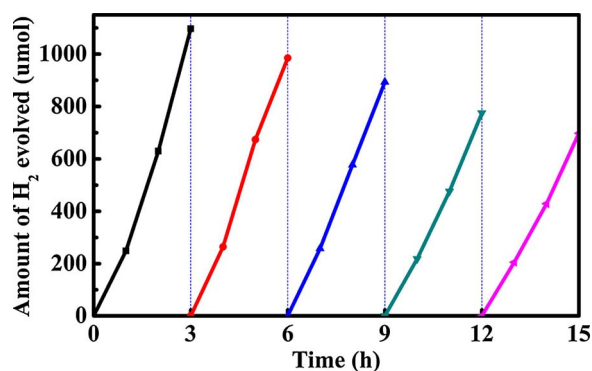
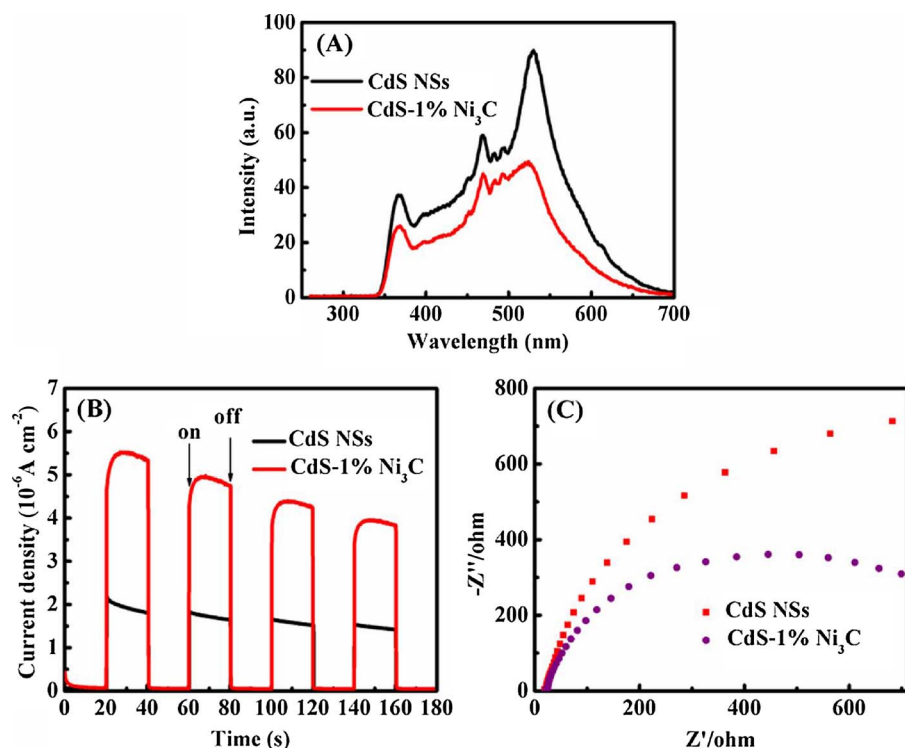


Fig. 8. Repeated time courses of photocatalytic H<sub>2</sub> evolution over CdS-1%Ni<sub>3</sub>C sample in 0.25 M Na<sub>2</sub>S-Na<sub>2</sub>SO<sub>3</sub> aqueous solution.



**Fig. 9.** (A) Photoluminescence spectra of CdS NSs and CdS-1%Ni<sub>3</sub>C photocatalysts with an excitation wavelength of 230 nm. (B) Transient photocurrent responses (*I*-*t* curves) of CdS NSs and CdS-1%Ni<sub>3</sub>C photocatalysts in 0.1 M Na<sub>2</sub>SO<sub>4</sub> aqueous solution under visible light irradiation at 0.1 V vs Ag/AgCl. (C) Nyquist plots of different working electrodes in 0.1 M Na<sub>2</sub>S and 0.02 M Na<sub>2</sub>SO<sub>3</sub> mixed aqueous solutions in the dark.

the important parameters in determining the photocatalytic H<sub>2</sub> evolution.

Electrochemical impedance spectra (EIS) measurements were employed to deeply study the separation efficiency of electron-hole pairs and the charge transfer resistance at solid/electrolyte interfaces. The Nyquist plots of the photocatalysts were shown in Fig. 9C. Clearly, the semicircle radius of CdS-1%Ni<sub>3</sub>C composite photocatalyst was much smaller than that of pure CdS NSs, suggesting that the loading of 1% Ni<sub>3</sub>C cocatalysts could effectively decrease the interface charge transfer resistance and improve the separation efficiency of photogenerated charge carriers.

As displayed in Fig. 10, the fluorescence lifetime measurements were used to further investigate the separation and transfer processes of photo-generated charge carriers. The average lifetime was calculated using the following equation [79]:

$$\langle t \rangle = (A_1 \tau_1^2 + A_2 \tau_2^2) / (A_1 \tau_1 + A_2 \tau_2)$$

Where  $\tau_1$  and  $\tau_2$  represent the emission lifetimes, and  $A_1$  and  $A_2$  are the corresponding amplitudes. The calculated average lifetimes of CdS NSs, CdS-1%Ni<sub>3</sub>C were 1.4486 and 5.1865 ns, respectively. Clearly, the average lifetime of CdS-1% Ni<sub>3</sub>C is much longer than that of pure CdS NSs. The test results show that loading the Ni<sub>3</sub>C on the surface of CdS NSs can significantly increase the average fluorescence lifetime, thus achieving the efficiently improved electron transfer between the Ni<sub>3</sub>C

and CdS NSs, which are beneficial for enhancing the photocatalytic H<sub>2</sub> evolution.

### 3.5. Discussion of mechanism

Mott-Schottky (MS) plots were used to estimate the flat-band ( $V_{fb}$ ) positions of the CdS NSs and CdS-1%Ni<sub>3</sub>C at 1 kHz in Na<sub>2</sub>SO<sub>4</sub> (0.1 M). As showed in Fig. 11, the positive tangent slopes of the straight lines revealed that CdS was an n-type inorganic semiconductor. The flat band potentials for CdS NSs and CdS-1%Ni<sub>3</sub>C can be approximately estimated to be -1.07 and -1.00 V (vs Ag/AgCl), respectively. The CdS-1%Ni<sub>3</sub>C sample shows a clearly positive shift of the flat-band potential compared to that of pure CdS NSs. Although  $V_{fb}$  value is difference from the conduction band potential, these results could also indicated the similar positive shift of conduction band edge of Ni<sub>3</sub>C/CdS, compared to that of CdS NSs. Thus, the positive shift implies the formation of strong interactions between Ni<sub>3</sub>C and CdS, which is beneficial for promoting the efficient photoelectron transfer between CdS and Ni<sub>3</sub>C.

According to the valence-band XPS analysis (Fig. 12A and B), the valence band maximum (VBM) positions for CdS NSs and CdS-1%Ni<sub>3</sub>C could be estimated to be 1.52 and 1.41 V (versus NHE), respectively. The corresponding CBM position could be calculated according to the band gap energy and VBM position. The specific electronic band structures of two different photocatalysts were displayed in Fig. 12C. As

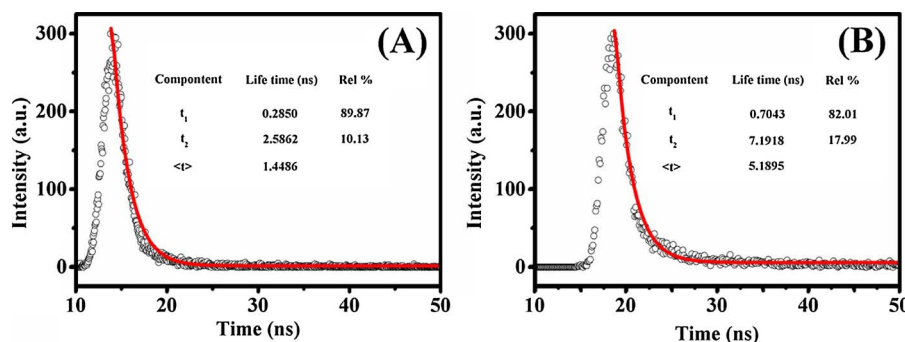


**Fig. 10.** Time-resolved transient PL decay of (A) CdS NSs, (B) CdS-1%Ni<sub>3</sub>C.



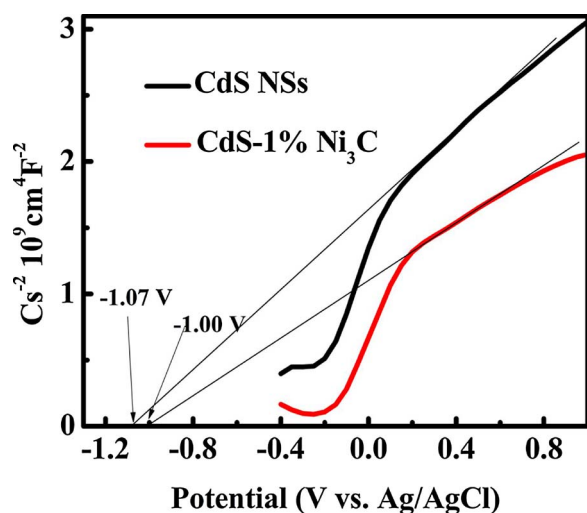


Fig. 11. Mott-Schottky (MS) plots of pure CdS NSs and CdS-1%Ni<sub>3</sub>C. The MS plots were measured at 1 kHz in Na<sub>2</sub>SO<sub>4</sub> (0.1 M).

as a result, it is clear that the loading of 1% Ni<sub>3</sub>C NPs leads to the reduced CB and VB levels, which are consistent with the results obtained in Fig. 11 and unfavorable for improving the photocatalytic H<sub>2</sub> evolution under visible-light irradiation. Nevertheless, the loading of 1% Ni<sub>3</sub>C NPs could also effectively narrow the band gap of CdS NSs for enhancing visible-light absorbance, thus favoring the photocatalytic H<sub>2</sub> evolution.

To further highlight the key roles of Ni<sub>3</sub>C cocatalysts in improving the photocatalytic H<sub>2</sub> evolution performance, polarization curves of CdS NSs, Ni<sub>3</sub>C NPs, CdS-1%Ni<sub>3</sub>C and Pt/C photocatalysts were carried out in the potential range of −1.2 to 0.2 V vs NHE. As displayed in Fig. 13A, the observed cathodic current ranging from −0.3 to −1.0 V versus NHE can be attributed to the electrocatalytic H<sub>2</sub> evolution. Obviously, the pure Ni<sub>3</sub>C NPs and Pt/C cocatalysts show the much lower electrocatalytic H<sub>2</sub>-evolution overpotentials than those of CdS NSs and CdS-1%Ni<sub>3</sub>C, indicating that Ni<sub>3</sub>C NPs could act as cocatalysts to efficiently improve the electrocatalytic H<sub>2</sub>-evolution kinetics and decrease

the overpotential in 0.5 M H<sub>2</sub>SO<sub>4</sub> solution. Similarly, in the aqueous electrolyte solution of 0.25 M Na<sub>2</sub>S–Na<sub>2</sub>SO<sub>3</sub> or 10 vol% lactic acid, the same conclusion can be drawn in Fig. 13B and C. Meanwhile, compared with 0.25 M Na<sub>2</sub>S–Na<sub>2</sub>SO<sub>3</sub> aqueous solution, the pure CdS NSs and CdS-1%Ni<sub>3</sub>C exhibited much lower electrocatalytic H<sub>2</sub>-evolution overpotentials in 10 vol% lactic acid solution, which might lead to the better photocatalytic H<sub>2</sub>-evolution activity. Therefore, the noble-metal-free Ni<sub>3</sub>C NPs as H<sub>2</sub>-evolution electrocatalysts are thoroughly verified, implying that the Ni<sub>3</sub>C NPs should be promising cocatalysts for water splitting, which are consistent with the recent reports about the simultaneously improved H<sub>2</sub> evolution [67,69]. According to the photocatalytic mechanism, the Ni<sub>3</sub>C NPs as active sites over CdS NSs play the crucial role in decreasing the H<sub>2</sub>-evolution overpotentials and improving the H<sub>2</sub>-evolution kinetics, thus directly enhancing photocatalytic H<sub>2</sub> evolution.

Based on the aforementioned results and discussion, the tentative reaction mechanism of photocatalytic H<sub>2</sub> evolution over the Ni<sub>3</sub>C/CdS NSs composites under visible light irradiation was proposed as illustrated in Scheme 2. Under irradiation, the electrons were readily excited from the valence band (VB) to conduction band (CB) of CdS NSs and then reacted with the H<sup>+</sup> ions to form H<sub>2</sub>. However, the rapid recombination of photo-generated electron-hole pairs in CdS NSs leads to their relatively low activity for photocatalytic H<sub>2</sub> evolution. By the contrary, for the Ni<sub>3</sub>C/CdS composite photocatalysts, the photo-generated electrons could quickly transfer to noble-metal-free Ni<sub>3</sub>C cocatalysts through the interface contact between CdS NSs and Ni<sub>3</sub>C NPs due to its high electrical conductivity and low electrocatalytic H<sub>2</sub>-evolution overpotential, then achieving the effective separation of the photo-generated electron-hole pairs and prolonged charge-carrier lifetime. Meanwhile, the holes on the VB of CdS NSs with strong oxidation ability could be rapidly removed by the Na<sub>2</sub>S/Na<sub>2</sub>SO<sub>3</sub> under visible light irradiation, therefore further promoting the photocatalytic H<sub>2</sub>-evolution activity. As a result, loading noble-metal-free Ni<sub>3</sub>C cocatalysts on the surface of CdS NSs can effectively boost the separation of photo-generated electron-hole pairs and accelerate the H<sub>2</sub>-evolution kinetics, thus achieving the significantly improved photocatalytic H<sub>2</sub>-evolution activity over the Ni<sub>3</sub>C/CdS NSs composite photocatalysts.

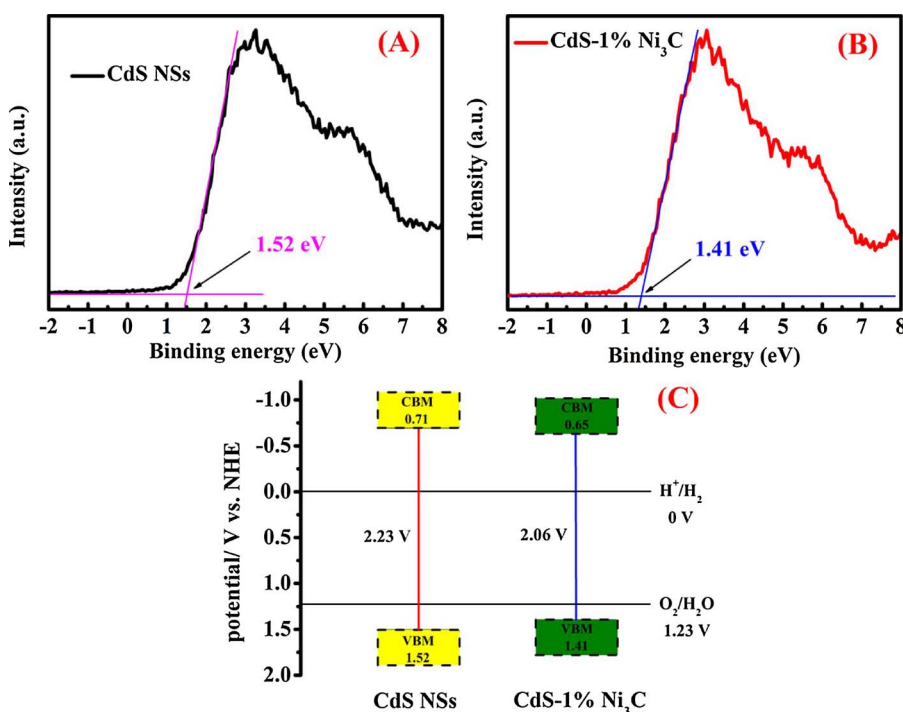


Fig. 12. Valence-band XPS spectra of (A) CdS NSs, (B) CdS-1%Ni<sub>3</sub>C, (C) the corresponding band gap structures of two photocatalysts.

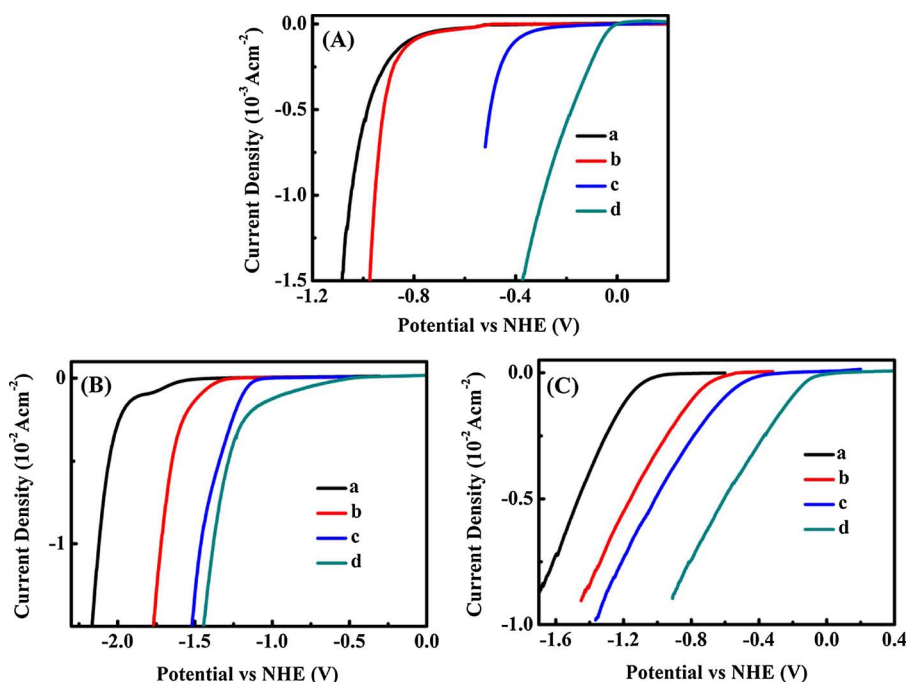
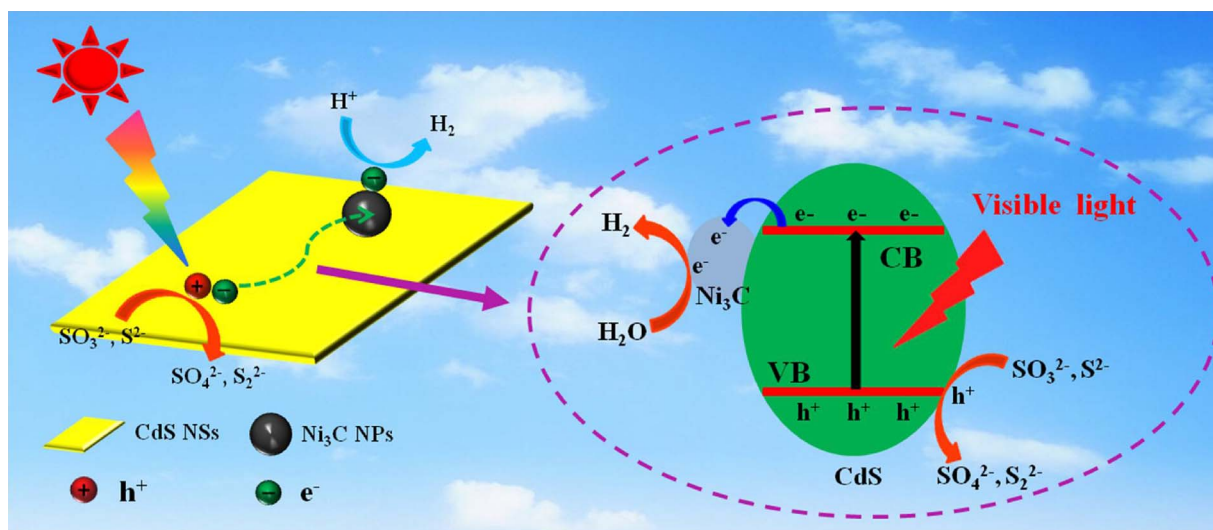


Fig. 13. Polarization curves of the photocatalysts were measured at a scan rate of  $5 \text{ mV s}^{-1}$  in 0.5 M  $\text{H}_2\text{SO}_4$  solution (A), 0.25 M  $\text{Na}_2\text{S-Na}_2\text{SO}_3$  aqueous solution (B), 10 vol% lactic acid solution (C).



Scheme 2. Proposed photocatalytic  $\text{H}_2$  evolution and charge transfer mechanisms in the binary  $\text{Ni}_3\text{C/CdS}$  NSs composite photocatalyst under visible light irradiation.

#### 4. Conclusions

In this study, the binary  $\text{Ni}_3\text{C/CdS}$  NSs composite photocatalysts were successfully synthesized by a facile grinding method. All the results demonstrated that the as-synthesized  $\text{CdS-1\%Ni}_3\text{C}$  composite exhibited the highest visible-light photocatalytic  $\text{H}_2$ -evolution rates of 357 and  $450.5 \mu\text{mol h}^{-1}$  in 0.25 M  $\text{Na}_2\text{S-Na}_2\text{SO}_3$  and lactic acid, which were about 7.76 and 4.79 times higher than that of pure CdS NSs, respectively. Clearly, the  $\text{Ni}_3\text{C}$  NPs can serve as  $\text{H}_2$ -evolution electrocatalysts either in acidic or basic media. It is believed that loading noble-metal-free  $\text{Ni}_3\text{C}$  NPs cocatalyst on the surface of CdS NSs can effectively increase the visible-light absorbance, promote the charge carriers separation and transfer, improve the surface  $\text{H}_2$ -evolution kinetics, thus achieving the obviously enhanced hydrogen evolution. This study indicates that  $\text{Ni}_3\text{C}$  NPs as a noble-metal-free cocatalysts show the great potential for enhancing visible light photocatalytic  $\text{H}_2$  evolution. It is also highly hoped that the  $\text{Ni}_3\text{C}$  cocatalysts can be widely used in visible light photocatalytic  $\text{H}_2$  evolution over other semiconductors.

#### Acknowledgements

The work was supported by National Natural Science Foundation of China (51672089), Special Funding on Applied Science and Technology in Guangdong (2017B020238005) and the State Key Laboratory of Advanced Technology for Material Synthesis and Processing (Wuhan University of Technology) (2015-KF-7).

#### References

- [1] X. Li, J. Yu, J. Low, Y. Fang, J. Xiao, X. Chen, *J. Mater. Chem. A* 3 (2015) 2485–2534.
- [2] A. Fujishima, K. Honda, *Nature* 238 (1972) 37–38.
- [3] J. Wen, J. Xie, X. Chen, X. Li, *Appl. Surf. Sci.* 391 (2017) 72–123.
- [4] J. Wen, X. Li, W. Liu, Y. Fang, J. Xie, Y. Xu, *Chin. J. Catal.* 36 (2015) 2049–2070.
- [5] Q. Li, X. Li, S. Wageh, A.A. Al-Ghamdi, J. Yu, *Adv. Energy Mater.* 5 (2015) 1500010.
- [6] X.F. Ning, J. Li, B.J. Yang, W.L. Zhen, Z. Li, B. Tian, G.X. Lu, *Appl. Catal. B-Environ.* 212 (2017) 129–139.
- [7] Q.J. Xiang, B. Cheng, J.G. Yu, *Appl. Catal. B-Environ.* 138 (2013) 299–303.

- [8] D. Lang, Q.J. Xiang, G.H. Qiu, X.H. Feng, F. Liu, *Dalton Trans.* 43 (2014) 7245–7253.
- [9] J. Yu, Y. Yu, P. Zhou, W. Xiao, B. Cheng, *Appl. Catal. B-Environ.* 156 (2014) 184–191.
- [10] J. Yu, Y. Yu, B. Cheng, *Rsc. Adv.* 2 (2012) 11829–11835.
- [11] Z.K. Yue, A.J. Liu, C.Y. Zhang, J. Huang, M.S. Zhu, Y.K. Du, P. Yang, *Appl. Catal. B-Environ.* 201 (2017) 202–210.
- [12] J.-J. Zhou, R. Wang, X.-L. Liu, F.-M. Peng, C.-H. Li, F. Teng, Y.-P. Yuan, *Appl. Surf. Sci.* 346 (2015) 278–283.
- [13] F.Y. Cheng, H. Yin, Q.J. Xiang, *Appl. Surf. Sci.* 391 (2017) 432–439.
- [14] J.Z. Su, T. Zhang, L. Wang, J.W. Shi, Y.B. Chen, *Chin. J. Catal.* 38 (2017) 489–497.
- [15] H. Du, Y.N. Liu, C.C. Shen, A.W. Xu, *Chin. J. Catal.* 38 (2017) 1295–1306.
- [16] J. Zhang, S.Z. Qiao, L. Qi, J. Yu, *Phys. Chem. Chem. Phys.* 15 (2013) 12088–12094.
- [17] F.Q. Zhou, J.C. Fan, Q.J. Xu, Y.L. Min, *Appl. Catal. B-Environ.* 201 (2017) 77–83.
- [18] X. Jia, M. Tahir, L. Pan, Z.F. Huang, X.W. Zhang, L. Wang, J.J. Zou, *Appl. Catal. B-Environ.* 198 (2016) 154–161.
- [19] Y. Huang, Y. Liu, D. Zhu, Y. Xin, B. Zhang, *J. Mater. Chem. A* 4 (2016) 13626–13635.
- [20] L.J. Zhang, S. Li, B.K. Liu, D.J. Wang, T.F. Xie, *ACS Catal.* 4 (2014) 3724–3729.
- [21] A.Y. Meng, B.C. Zhu, B. Zhong, L.Y. Zhang, B. Cheng, *Appl. Surf. Sci.* 422 (2017) 518–527.
- [22] Y.G. Lei, C. Yang, J.H. Hou, F. Wang, S.X. Min, X.H. Ma, Z.L. Jin, J. Xu, G.X. Lu, K.W. Huang, *Appl. Catal. B-Environ.* 216 (2017) 59–69.
- [23] C. Zhu, C.G. Liu, Y.J. Zhou, Y.J. Fu, S.J. Guo, H. Li, S.Q. Zhao, H. Huang, Y. Liu, Z.H. Kang, *Appl. Catal. B-Environ.* 216 (2017) 114–121.
- [24] Q. Li, B. Guo, J. Yu, J. Ran, B. Zhang, H. Yan, J.R. Gong, *J. Am. Chem. Soc.* 133 (2011) 10878–10884.
- [25] X. Li, J. Yu, S. Wageh, A.A. Al-Ghamdi, J. Xie, *Small* 12 (2016) 6640–6696.
- [26] T. Di, B. Zhu, J. Zhang, B. Cheng, J. Yu, *Appl. Surf. Sci.* 389 (2016) 775–782.
- [27] D. Lang, F.Y. Cheng, Q.J. Xiang, *Catal. Sci. Technol.* 6 (2016) 6207–6216.
- [28] W. Zhang, Y. Wang, Z. Wang, Z. Zhong, R. Xu, *Chem. Commun.* 46 (2010) 7631–7633.
- [29] Q.J. Xiang, F.Y. Cheng, D. Lang, *ChemSusChem* 9 (2016) 996–1002.
- [30] Y. Xu, W.G. Tu, S.M. Yin, M. Kraft, Q.C. Zhang, R. Xu, *Dalton Trans.* 46 (2017) 10650–10656.
- [31] Z. Fang, Y. Wang, J. Song, Y. Sun, J. Zhou, R. Xu, H. Duan, *Nanoscale* 5 (2013) 9830–9838.
- [32] S. Yin, J. Han, Z. Yinjun, T. Zhou, R. Xu, *Nanoscale* 8 (2016) 14438–14447.
- [33] Q. Li, H. Meng, P. Zhou, Y. Zheng, J. Wang, J. Yu, J. Gong, *ACS Catal.* 3 (2013) 882–889.
- [34] D. Lang, T.T. Shen, Q.J. Xiang, *ChemCatChem* 7 (2015) 943–951.
- [35] X. Li, J. Yu, M. Jaroniec, *Chem. Soc. Rev.* 45 (2016) 2603–2636.
- [36] S. Ma, J. Xie, J. Wen, K. He, X. Li, W. Liu, X. Zhang, *Appl. Surf. Sci.* 391 (2017) 580–591.
- [37] Y. Xu, X. Yin, Y. Huang, P. Du, B. Zhang, *Chem. – Eur. J.* 21 (2015) 4571–4575.
- [38] M. Zhukovskiy, P. Tongying, H. Yashan, Y. Wang, M. Kuno, *ACS Catal.* 5 (2015) 6615–6623.
- [39] N. Bao, L. Shen, T. Takata, K. Domen, *Chem. Mater.* 20 (2008) 110–117.
- [40] Y. Xu, W. Zhao, R. Xu, Y. Shi, B. Zhang, *Chem. Commun.* 49 (2013) 9803–9805.
- [41] H. Yan, J. Yang, G. Ma, G. Wu, X. Zong, Z. Lei, J. Shi, C. Li, *J. Catal.* 266 (2009) 165–168.
- [42] T. Simon, N. Bouchonville, M.J. Berr, A. Vaneski, A. Adrovic, D. Volbers, R. Wyrwich, M. Döblinger, A.S. Sussha, A.L. Rogach, *Nat. Mater.* 13 (2014) 1013.
- [43] Q.X. Peng, D. Xue, S.Z. Zhan, C.L. Ni, *Appl. Catal. B-Environ.* 219 (2017) 353–361.
- [44] X.L. Yin, L.L. Li, W.J. Jiang, Y. Zhang, X. Zhang, L.J. Wan, J.S. Hu, *ACS Appl. Mater. Interfaces* 8 (2016) 15258–15266.
- [45] K. Chang, M. Li, T. Wang, S. Ouyang, P. Li, L. Liu, J. Ye, *Adv. Energy Mater.* 5 (2015) 1402279.
- [46] X. Zong, H. Yan, G. Wu, G. Ma, F. Wen, L. Wang, C. Li, *J. Am. Chem. Soc.* 130 (2008) 7176–7177.
- [47] B. Han, S.Q. Liu, N. Zhang, Y.J. Xu, Z.R. Tang, *Appl. Catal. B-Environ.* 202 (2017) 298–304.
- [48] A.P. Wu, C.G. Tian, Y.Q. Jiao, Q. Yan, G.Y. Yang, H.G. Fu, *Appl. Catal. B-Environ.* 203 (2017) 955–963.
- [49] Y.G. Lei, J.H. Hou, F. Wang, X.H. Ma, Z.L. Jin, J. Xu, S.X. Min, *Appl. Surf. Sci.* 420 (2017) 456–464.
- [50] J.J. Zhang, W.S. Li, Y. Li, L. Zhong, C.J. Xu, *Appl. Catal. B-Environ.* 217 (2017) 30–36.
- [51] S. Hong, D.P. Kumar, D.A. Reddy, J. Choi, T.K. Kim, *Appl. Surf. Sci.* 396 (2017) 421–429.
- [52] J. Yuan, J. Wen, Y. Zhong, X. Li, Y. Fang, S. Zhang, W. Liu, *J. Mater. Chem. A* 3 (2015) 18244–18255.
- [53] X. Zong, J. Han, G. Ma, H. Yan, G. Wu, C. Li, *J. Phys. Chem. C* 115 (2011) 12202–12208.
- [54] Y.Y. Zhong, G. Zhao, F.K. Ma, Y.Z. Wu, X.P. Hao, *Appl. Catal. B-Environ.* 199 (2016) 466–472.
- [55] S. Cao, Y. Chen, C.-J. Wang, P. He, W.-F. Fu, *Chem. Commun.* 50 (2014) 10427–10429.
- [56] Z.J. Sun, H.F. Zheng, J.S. Li, P.W. Du, *Energy Environ. Sci.* 8 (2015) 2668–2676.
- [57] Z.J. Sun, B.H. Lv, J.S. Li, M. Xiao, X.Y. Wang, P.W. Du, *J. Mater. Chem. A* 4 (2016) 1598–1602.
- [58] Y.M. Dong, L.G. Kong, G.L. Wang, P.P. Jiang, N. Zhao, H.Z. Zhang, *Appl. Catal. B-Environ.* 211 (2017) 245–251.
- [59] H.L. Chen, D.C. Jiang, Z.J. Sun, R.M. Irfan, L. Zhang, P.W. Du, *Catal. Sci. Technol.* 7 (2017) 1515–1522.
- [60] Z.J. Sun, H.L. Chen, L. Zhang, D.P. Lu, P.W. Du, *J. Mater. Chem. A* 4 (2016) 13289–13295.
- [61] J. Yuan, J. Wen, Q. Gao, S. Chen, J. Li, X. Li, Y. Fang, *Dalton Trans.* 44 (2015) 1680–1689.
- [62] Z. Yan, X. Yu, A. Han, P. Xu, P. Du, *J. Phys. Chem. C* 118 (2014) 22896–22903.
- [63] Z.P. Yan, Z.J. Sun, X. Liu, H.X. Jia, P.W. Du, *Nanoscale* 8 (2016) 4748–4756.
- [64] K. He, J. Xie, Z. Yang, R. Shen, Y. Fang, S. Ma, X. Chen, X. Li, *Catal. Sci. Technol.* 7 (2017) 1193–1202.
- [65] B.J. Ma, H.J. Xu, K.Y. Lin, J. Li, H.J. Zhan, W.Y. Liu, C. Li, *ChemSusChem* 9 (2016) 820–824.
- [66] J.R. Ran, G.P. Gao, F.T. Li, T.Y. Ma, A.J. Du, S.Z. Qiao, *Nat. Commun.* 8 (2017) 13907.
- [67] H. Yang, S. Luo, X. Li, S. Li, J. Jin, J. Ma, *J. Mater. Chem. A* 4 (2016) 18499–18508.
- [68] X.J. Fan, Z.W. Peng, R.Q. Ye, H.Q. Zhou, X. Guo, *ACS Nano* 9 (2015) 7407–7418.
- [69] H. Wang, Y.J. Cao, G.F. Zou, Q.H. Yi, J. Guo, L.J. Gao, *ACS Appl. Mater. Interfaces* 9 (2017) 60–64.
- [70] Y. Goto, K. Taniguchi, T. Omata, S. Otsuka-Yao-Matsuo, N. Ohashi, S. Ueda, H. Yoshikawa, Y. Yamashita, H. Oohashi, K. Kobayashi, *Chem. Mater.* 20 (2008) 4156–4160.
- [71] R. Bera, S. Kundu, A. Patra, *ACS Appl. Mater. Interfaces* 7 (2015) 13251–13259.
- [72] R.-T. Chiang, R.-K. Chiang, F.-S. Shieu, *RSC Adv.* 4 (2014) 19488.
- [73] J. He, L. Chen, F. Wang, Y. Liu, P. Chen, C.T. Au, S.F. Yin, *ChemSusChem* 9 (2016) 624–630.
- [74] M. Thommes, K. Kaneko, A.V. Neimark, J.P. Olivier, F. Rodriguez-Reinoso, J. Rouquerol, K.S. Sing, *Pure Appl. Chem.* 87 (2015) 1051–1069.
- [75] J. Xu, X. Cao, *J. Chem. Eng.* 260 (2015) 642–648.
- [76] S. Cao, Y. Chen, C.-C. Hou, X.-J. Lv, W.-F. Fu, *J. Mater. Chem. A* 3 (2015) 6096–6101.
- [77] K. He, J. Xie, X. Luo, J. Wen, S. Ma, X. Li, Y. Fang, X. Zhang, *Chin. J. Catal.* 38 (2017) 240–252.
- [78] L. Pan, J.W. Zhang, X. Jia, Y.H. Ma, X.W. Zhang, L. Wang, J.J. Zou, *Chin. J. Catal.* 38 (2017) 253–259.
- [79] Z. Zhang, J. Huang, M. Zhang, Q. Yuan, B. Dong, *Appl. Catal. B-Environ.* 163 (2015) 298–305.